

* You need to say why you are introducing a new test case. Eg:
as a challenge to cut cells in situations with large Froude number and large
Scorer parameter

Comparison of Terrain Following and Cut Cell Grids using a Non-Hydrostatic Model

JAMES SHAW* AND HILARY WELLER

Department of Meteorology, University of Reading, Reading, United Kingdom

** As expected, the cut cell grid maintains stationary, stratified flow more
accurately.

ABSTRACT

Terrain following coordinates are widely used in operational models but the cut cell method has been proposed as an alternative that can more accurately represent the orography and associated atmospheric dynamics. Because the type of grid is usually chosen during model implementation, it is typically necessary to use different models in order to compare the accuracy of different grids. On the contrary, we use a single C-grid finite volume model to enable a like-for-like comparison of terrain following and cut cell grids. A series of standard two-dimensional tests using idealised terrain are performed: tracer advection in a prescribed horizontal velocity field, a test of a stably stratified atmosphere at rest, and orographically induced gravity waves. In addition, we formulate a new tracer advection test having a velocity field that is everywhere tangential to the terrain following coordinate surfaces.*The results of the advection tests demonstrate that tracer accuracy depends upon alignment of the flow with the grid. In the gravity waves test, results on all grids are in good agreement with existing results from the literature.** However, we find that the Lorenz computational mode is excited as a vertical zig-zag in potential temperature on the cut cell grid.

xx from the heat release due to convection and the forcing of gravity
and Rossby waves. But what did John think of this intro. More his field
when simulating orographically induced
gravity waves.

1. Introduction

Representing orography accurately in numerical weather prediction systems is necessary to model downslope winds and local precipitation. Orography also exerts strong non-local influences ~~by the atmospheric response to form drag and gravity wave drag~~. There are two main approaches to represent orography on a grid: terrain following layers and cut cells. Both methods align cells in vertical columns. Because most models are designed for a particular type of grid, existing studies of cut cell solutions have compared results with terrain following grid solutions implemented within different models, for example Good et al. (2014). Instead, this study uses a single model to enable a like-for-like comparison between solutions using terrain following and cut cell grids.

xx

With increasing horizontal model resolution, the discrete representation of terrain can become steeper, making accurate calculation of the horizontal pressure gradient more difficult when using terrain following layers (Gary 1973; Steppeler et al. 2002). Numerical errors in this calculation result in spurious winds and can cause numerical instability (Fast 2003; Webster et al. 2003). Cut cell methods seek to reduce the error that is associated with steep orography.

With terrain following (TF) layers the terrain's influence decays with height so that the bottommost layers fol-

low the underlying surface closely while the uppermost layers are flat. There are two main approaches to minimizing errors associated with TF layers. First, by smoothing the effects of terrain with height, the influence of the terrain is reduced, hence errors in the calculated horizontal pressure gradient are also reduced aloft (Schär et al. 2002; Leuenberger et al. 2010; Klemp 2011). However, the error is not reduced at the ground where steep terrain remains unmodified.

Second, numerical errors can also be reduced by improving the accuracy in calculating the horizontal pressure gradient itself. TF layers are usually implemented using a coordinate transformation onto a rectangular computational domain, which introduces metric terms into the equations of motion. The techniques proposed by Klemp (2011) and Zängl (2012) both involve the calculation of the horizontal pressure gradient in the physical domain. This gave them the flexibility to design more accurate horizontal pressure gradient discretizations using more appropriate stencils.

Despite their associated numerical errors, TF layers are in widespread operational use (Steppeler et al. 2003). They are attractive because their rectangular structure is simple to process by computer, boundary layer resolution can be increased with variable spacing of vertical layers (Schär et al. 2002), and cell sizes remain almost constant (Jebens et al. 2011).

Cut cells is an alternative method in which the grid does not follow the terrain but, instead, cells that lie entirely

* Corresponding author address: Department of Meteorology, University of Reading, Earley Gate, PO Box 243, Reading, RG6 6BB, UK.
E-mail: js102@zepler.net

below the terrain are removed, and those that intersect the surface are modified in shape so that they more closely fit the terrain. The resulting grid is orthogonal everywhere except near cells that have been cut. Hence, errors are still introduced when calculating the horizontal pressure gradient between cut and uncut cells.

The cut cell method can create some very small cells which reduce computational efficiency (Klein et al. 2009), and several approaches have been tried to alleviate the problem (Steppeler et al. 2002; Yamazaki and Satomura 2010; Jebens et al. 2011).

Several studies have shown examples where cut cells produce more accurate results when compared to TF coordinates. Spurious winds seen in TF coordinates are not present and errors do not increase with steeper terrain (Good et al. 2014). A comparison of TF and cut cells using real initial data by Steppeler et al. (2013) found that precipitation and wind forecasts were more accurately in the cut cell model.

This study uses the nonhydrostatic model from Weller and Shahrokhi (2014) to enable a like-for-like comparison between terrain following and cut cell grids for idealised, two-dimensional test cases from the literature. Section 2 presents the formulation of the terrain following and cut cell grids used in the experiments that follow. In section 3 we outline the model from Weller and Shahrokhi (2014) and the governing equations. Section 4 analyses the results from two tracer advection tests, a test of a stably stratified atmosphere initially at rest, and orographically induced gravity waves. Concluding remarks are made in section 5.

2. Grids

Here we describe the formulation of the terrain following grids and the method of cut cell grid construction. The techniques presented are used to define the grids for the experiments in the subsequent section.

Gal-Chen and Somerville (1975) proposed a basic terrain following (BTF) coordinate defined as

$$z = (H - h)(z^*/H) + h \quad (1)$$

where, in two dimensions, $z(x, z^*)$ is the physical height of the coordinate surface at level z^* , H is the height of the domain, and $h(x)$ is the height of the terrain surface. This formulation results in z^*/H ranging from 0 to 1. Using this coordinate, the terrain's influence decays linearly with height but disappears only at the top of the domain. An example is shown in figure 1a.

The sigma coordinate transform of Phillips (1957) is equivalent to the BTF coordinate transform since they both decay linearly. However, because $\sigma = p/p_s$ decays with pressure rather than height, sigma coordinates also vary with surface pressure, $p_s(x, t)$.

The hybrid terrain following (HTF) coordinates of Simmons and Burridge (1981) improve upon BTF coordinates by using a decay function that allows the influence of the terrain to be removed at a specified height, producing flat model layers aloft.

The smooth level vertical (SLEVE) coordinate proposed by Schär et al. (2002) achieves a more regular TF grid in the middle and top of the domain than the BTF coordinate. The terrain height is split into large-scale and small-scale components, h_1 and h_2 , such that $h = h_1 + h_2$, with each component having a different exponential decay. The transformation is defined as

$$z = z^* + h_1 b_1 + h_2 b_2 \quad (2)$$

where the vertical decay functions are given by

$$b_i = \frac{\sinh((H/s_i)^n - (z^*/s_i)^n)}{\sinh(H/s_i)^n} \quad (3)$$

with s_1 and s_2 are the scale heights of large-scale and small-scale terrain respectively. The exponent n was introduced by Leuenberger et al. (2010) in order to increase cell thickness in the layers nearest the ground, allowing longer timesteps and permitting more accurate calculation of parameterised low-level heat and momentum fluxes. Leuenberger et al. (2010) found the exponent has an optimal value of $n = 1.35$. Choosing $n = 1$ gives the decay functions used by Schär et al. (2002). An example of the SLEVE grid can be seen in figure 1b.

Most implementations of terrain following layers use a coordinate system that makes the domain rectangular, but introduces metric terms into the equations of motion. Instead, the model employed in this study uses Cartesian coordinates and unstructured grids. By doing so, results from the same model can be compared between terrain following and cut cell grids without modifying the equation set or discretisation.

The OpenFOAM utility `snappyHexMesh` was used to create a grid that approximates the cut cell method. First, a custom utility was used to move points beneath the surface up to the surface creating small cells near mountain peaks. The utility is available at <https://github.com/hertzprung/AtmosFOAM/tree/2386ffb/applications/utilities/mesh/add2dMountain>. Second, the surface faces were taken from the BTF grid and `snappyHexMesh` was used to intersect the surface with the grid. The tool removes cells whose centres are below the surface and displaces boundary vertices so that they are 'snapped' to the BTF surface (OpenCFD Foundation cited 2015). An example of the resulting grid is shown in figure 1c.

There are two details of grid construction which mean that resulting cut cell grids can differ slightly from a typical cut cell grid created using a shaving method, as described by Adcroft et al. (1997). First, when

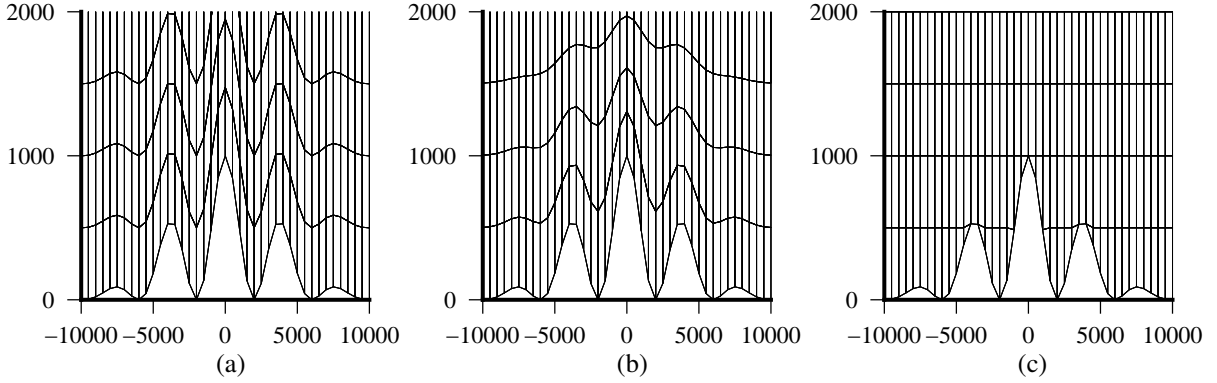


FIG. 1. Examples of (a) BTF, (b) SLEVE, and (c) a cut cell grid, showing cell edges in the lowest four layers. The two dimensional grids are 20 km wide and 20 km high. SLEVE parameters are specified in the resting atmosphere test in section 4c. The cut cell grid was created by intersecting the terrain surface with a regular grid as described in section 2.

snappyHexMesh moves vertices onto the terrain surface, some points are moved horizontally. Second, the utility does not create new points necessary for pentagonal cells.

Great description of the grid generation

3. Model

We use the finite volume model from Weller and Shahrokhi (2014) which details a C-grid discretisation of the fully-compressible Euler equations, given by

$$\text{Momentum} \quad \frac{\partial \rho \mathbf{u}}{\partial t} + \nabla \cdot \rho \mathbf{u} \mathbf{u} = \rho \mathbf{g} - c_p \rho \theta \nabla \Pi \quad (4a)$$

$$\text{Continuity} \quad \frac{\partial \rho}{\partial t} + \nabla \cdot \rho \mathbf{u} = 0 \quad (4b)$$

$$\theta, \text{ flux form} \quad \frac{\partial \rho \theta}{\partial t} + \nabla \cdot \rho \mathbf{u} \theta = 0 \quad (4c)$$

$$\text{not needed} \quad \theta, \text{ advective form} \quad \frac{\partial \theta}{\partial t} + \mathbf{u} \cdot \nabla \theta = 0 \quad (4d)$$

$$\text{Equation of state} \quad \Pi^{(1-\kappa)/\kappa} = \frac{R \rho \theta}{p_0} \quad (4e)$$

where ρ is the density, \mathbf{u} is the velocity field, \mathbf{g} is the gravitational acceleration, c_p is the heat capacity at constant pressure, $\theta = T(p_0/p)^\kappa$ is the potential temperature, T is the temperature, p is the pressure, p_0 is a reference pressure, $\Pi = (p/p_0)^\kappa$ is the Exner function of pressure, and $\kappa = R/c_p$ is the gas constant to heat capacity ratio.

The model has a curl-free pressure gradient formulation and an upwind-biased cubic advection scheme. It uses a Lorenz staggering of thermodynamic variables such that θ is stored at cell centres and velocity at cell faces.

This section is very short. Do you need to say something about how a staggered finite volume code relates to C-grid finite difference?

4. Results

A series of two-dimensional tests are performed over idealised orography. For each test, results on the BTF,

SLEVE and cut cell grid are compared. The first test from Schär et al. (2002) advects a tracer in a horizontal velocity field. Second, a new tracer advection test is formulated employing a terrain following velocity field to challenge the advection scheme on more orthogonal grids. The third test solves the Euler equations for a stably stratified atmosphere initially at rest, following Klemp (2011). Finally, as specified by Schär et al. (2002), a test of orographically-induced gravity waves is performed. No explicit diffusion is used in any of the tests.

a. Horizontal advection

Following Schär et al. (2002), a tracer is transported above wave-shaped terrain by solving the advection equation for a prescribed horizontal wind. This test challenges the accuracy of the advection scheme in the presence of grid distortions.

The domain is 301 km wide and 25 km high, discretized onto a grid with $\Delta x = 1$ km and $\Delta z^* = 500$ m. The domain specified by Schär et al. (2002) is 300 km between the outermost cell centres.* In order to reproduce the result from Schär et al. (2002), the domain has been extended horizontally by $\Delta x/2$ m in both directions so that the distance between the outermost cell centres is still 300 km.

The terrain is wave-shaped, specified by the surface height, h , such that

$$h(x) = h^* \cos^2(\alpha x) \quad (5a)$$

where

$$h^*(x) = \begin{cases} h_0 \cos^2(\beta x) & \text{if } |x| < a \\ 0 & \text{otherwise} \end{cases} \quad (5b)$$

where $a = 25$ km is the mountain envelope half-width, $h_0 = 3$ km is the maximum mountain height, $\lambda = 8$ km is the wavelength, $\alpha = \pi/\lambda$ and $\beta = \pi/2a$. On the

ie, what is a cell face. Where are scalars and velocity stored?

SLEVE grid, the large-scale component h_1 is given by $h_1(x) = h^*(x)/2$ and $s_1 = 15$ km is the large scale height, and $s_2 = 2.5$ km is the small scale height. The optimisation of SLEVE by Leuenberger et al. (2010) is not used, so the exponent $n = 1$.

The wind is entirely horizontal and is prescribed as

$$u(z) = u_0 \begin{cases} 1 & \text{if } z \geq z_2 \\ \sin^2\left(\frac{\pi}{2} \frac{z-z_1}{z_2-z_1}\right) & \text{if } z_1 < z < z_2 \\ 0 & \text{otherwise} \end{cases} \quad (6)$$

where $u_0 = 10 \text{ m s}^{-1}$, $z_1 = 4$ km and $z_2 = 5$ km. This results in a constant wind aloft, and zero flow at 4 km and below.

To ensure ^{that} the discrete velocity field is non-divergent, velocities are prescribed at cell faces by ^{differencing} summing the streamfunction, Ψ , ~~at the centre of all face edges~~. Since $u = -\partial\Psi/\partial z$, the streamfunction is found by vertical integration of the velocity profile:

along the edges from \Psi stored at cell vertices

$$\Psi(z) = \frac{u_0}{2} \begin{cases} (2z - z_1 - z_2) & \text{if } z > z_2 \\ z - z_1 - \frac{z_2 - z_1}{\pi} \sin\left(\pi \frac{z - z_1}{z_2 - z_1}\right) & \text{if } z_1 < z \leq z_2 \\ 0 & \text{if } z \leq z_1 \end{cases} \quad (7)$$

A tracer, ϕ , is positioned upstream above the height of the terrain. It has the shape

$$\phi(x, z) = \phi_0 \begin{cases} \cos^2\left(\frac{\pi r}{2}\right) & \text{if } r \leq 1 \\ 0 & \text{otherwise} \end{cases} \quad (8)$$

having radius, r , given by

$$r = \sqrt{\left(\frac{x - x_0}{A_x}\right)^2 + \left(\frac{z - z_0}{A_z}\right)^2} \quad (9)$$

where $A_x = 25$ km, $A_z = 3$ km are the horizontal and vertical half-widths respectively, and $\phi_0 = 1$ is the maximum magnitude of the anomaly. At $t = 0$ s, the anomaly is centred at $(x_0, z_0) = (-50 \text{ km}, 9 \text{ km})$ so that the anomaly is upwind of the mountain and well above the maximum terrain height of 3 km. Analytic solutions can be found by setting the anomaly centre such that $x_0 = ut$.

The flux form of the advection equation, $\partial\phi/\partial t + \nabla \cdot (u\phi) = 0$, is solved using the upwind-biased cubic advection scheme described by Weller and Shahrokhi (2014) which is non-monotonic and not flux corrected. The time derivative is solved using a three-stage, second order Runge-Kutta scheme:

$$\phi^* = \phi^{(n)} + \Delta t f(\phi^{(n)}) \quad (10)$$

$$\phi^{**} = \phi^{(n)} + \frac{\Delta t}{2} \left(f(\phi^{(n)}) + f(\phi^*) \right) \quad (11)$$

$$\phi^{(n+1)} = \phi^{(n)} + \frac{\Delta t}{2} \left(f(\phi^{(n)}) + f(\phi^{**}) \right) \quad (12)$$

where $f(\phi^{(n)}) = -\text{div}(u\phi^{(n)})$ at time level n .

Unlike Schär et al. (2002) who use periodic lateral boundaries, a fixed value of 0 is used at the inlet boundary and all other boundaries have zero gradient. Tests are integrated forward in time for 10000 s with a timestep of $\Delta t = 25$ s.

The test was executed on the BTF, SLEVE and cut cell grids, and on a regular grid with flat terrain using a centred linear scheme and the upwind-biased cubic scheme. Results were also obtained on BTF and SLEVE grids with the fourth order scheme from Schär et al. (2002) using a modified version of their Fortran code. The original version of the code interpolated the geometric height at cell vertices from values at adjacent half levels in order to calculate the streamfunction, $\Psi(z)$. The modified version used here directly calculates the height at vertices to enable comparisons with the finite volume model solutions.

Tracer contours at $t = 0$ s, 5000 s and 10000 s are shown in Figure 2. The results are compared on the BTF grid for the centred linear scheme (2a) and the fourth order scheme from Schär et al. (2002) (2c), and the upwind-biased cubic scheme on the cut cell grid (2b), and BTF grid (2d). Tracer errors at $t = 10000$ s are shown for the fourth order and upwind-biased cubic schemes in figures 2e and 2f respectively.

By $t = 10000$ s, the tracer suffers from diffusion and distortion on the BTF grid using the centred linear scheme and some artefacts remain above the mountain peak. Distortions are reduced by using the fourth order scheme from Schär et al. (2002) (figure 2c), but the computational mode is seen as a grid-scale oscillation that travels in the opposite direction to the wind (figure 2e). The results from the centred linear and fourth order schemes are slightly worse than the respective results from Schär et al. (2002) (their figure 6a and figure 8) because gradients in Ψ have not been removed by interpolation.

Using the upwind-biased cubic scheme, tracer magnitude and shape are well-preserved on all grids, both above the mountain at $t = 5000$ s and past the mountain at $t = 10000$ s. In this test, advection is most accurate on the cut cell grid (figure 2b) and regular grid (not shown). As found by Good et al. (2014), the result is the same on both grids. This is to be expected since the wind is zero in the region of the ground and flow aloft is aligned with the grids. On the BTF grid, the tracer is less distorted by the cubic upwind-biased scheme (figure 2d) compared to the centred linear scheme (figure 2a) or fourth order scheme (figure 2c).

Minimum and maximum tracer values and ℓ^2 error norms on the BTF, SLEVE, cut cell and regular grids are summarised in table 1, where the ℓ^2 error norm is defined as

$$\ell^2 = \sqrt{\frac{\sum_c (\phi - \phi_T)^2 \mathcal{V}_c}{\sum_c (\phi_T^2 \mathcal{V}_c)}} \quad (13)$$

The advection equation should be a numbered equation in section 3. The RK scheme should be described in section 3

Another's difference is that schar uses centered in time

where ϕ is the numerical tracer value, ϕ_T is the analytic value and \mathcal{V}_c is the cell volume.

The results of the cubic upwind-biased scheme on TF and regular grids are comparable with those for the fourth-order centred scheme from Schär et al. (2002). Error is largest on the BTF grid with $\ell^2 = 0.00791$ but significant reduced on the SLEVE grid with $\ell^2 = 0.00108$. The error is approximately halved by changing from the SLEVE grid to the cut cell grid. Tracer minima and maxima for the centred linear and fourth order schemes are lower than those presented by Schär et al. (2002) because no interpolation is used to calculate the streamfunction.

The centred linear scheme is sensitive to changes in the terrain profile: when the domain width is reduced to 300 km, the ℓ^2 error on the BTF grid rises from 0.0210 to 0.0318. The upwind-biased cubic scheme is less sensitive to the same change, with the ℓ^2 error decreasing from 0.00791 to 0.00767.

The results of the tracer advection test show that numerical errors are due to misalignment of the flow with the grid.* Using the upwind-biased cubic scheme, distortions in the grid do not significantly distort the tracer.

* or to grid distortions

b. Terrain following advection

In the horizontal advection test, results were more accurate where the flow was aligned with the grid layers, and distortions in the BTF grid led to increased errors. We formulate a new tracer advection test in which the velocity field is everywhere tangential to the basic terrain following coordinate surfaces. In this new test, flow is aligned with the BTF grid layers. Misalignment on the SLEVE and cut cell grids is designed to challenge the advection scheme.

The spatial domain, mountain profile, initial tracer profile and discretisation are the same as those in the horizontal tracer advection test. The velocity field is defined using a streamfunction, Ψ , so that the continuous velocity field is non-divergent and follows the BTF coordinate surfaces given by equation 1 such that

$$\Psi(x, z) = -u_0 H \frac{z - h}{H - h} \quad (14)$$

where $u_0 = 10 \text{ m s}^{-1}$, which is the horizontal wind speed where $h(x) = 0$. The horizontal and vertical components of velocity, u and w , are then given by

$$u = -\frac{\partial \Psi}{\partial z} = -u_0 \frac{H}{H - h}, \quad w = \frac{\partial \Psi}{\partial x} = u_0 H \frac{dh}{dx} \frac{z - H}{(H - h)^2},$$

$$\frac{\partial h}{\partial x} = -h_0 [\beta \cos^2(\alpha x) \sin(2\beta x) + \alpha \cos^2(\beta x) \sin(2\alpha x)] \quad (15)$$

Unlike the horizontal advection test, flow extends from the top of the domain all the way to the ground. The discrete

velocity field is calculated using the streamfunction in the same way as the horizontal advection test.

At $t = 10000 \text{ s}$ the tracer has passed over the mountain. The horizontal position of the tracer centre can be calculated by integrating along the trajectory to find t , the time taken to pass from one side of the mountain to the other:

$$dt = dx/u(x) \quad (16)$$

$$t = \int_0^x \frac{H - h(x)}{u_0 H} dx \quad (17)$$

$$t = \frac{x}{u_0} - \frac{h_0}{16u_0 H} \left[4x + \frac{\sin 2(\alpha + \beta)x}{\alpha + \beta} + \frac{\sin 2(\alpha - \beta)x}{\alpha - \beta} + 2 \left(\frac{\sin 2\alpha x}{\alpha} + \frac{\sin 2\beta x}{\beta} \right) \right] \quad (18)$$

Hence, we find that $x(t = 10000 \text{ s}) = 51577.4 \text{ m}$. Because the velocity field is non-divergent, the flow accelerates over mountain ridges and the tracer travels 1577.4 m further compared to advection in the purely horizontal velocity field. Tracer height is unchanged downwind of the mountains because advection is along the terrain following coordinate surface.

ℓ^2 errors and tracer extrema for this test are compared with the horizontal advection results in table 1. In the terrain following velocity field, tracer accuracy is greatest on the BTF grid. Using the cubic upwind-biased scheme, errors are about ten times larger on the SLEVE and cut cell grids compared to the BTF grid.

We conclude from this test that accuracy depends upon alignment of the flow with the grid, and accuracy is not significantly reduced by grid distortions. Error on the BTF grid in the terrain following advection test is comparable with the error on the SLEVE grid in the horizontal advection test.

c. Stratified atmosphere initially at rest

An idealised terrain profile is defined along with a stably stratified atmosphere at rest in hydrostatic balance. The analytic solution is time-invariant, but numerical errors in calculating the horizontal pressure gradient can give rise to spurious velocities which become more severe over steeper terrain (Klemp 2011).

The test setup follows the specification by Klemp (2011), but has a narrower domain that is 20 km wide and 20 km high in order to reduce simulation time, as used by Weller and Shakhrokh (2014). The grid resolution is $\Delta x = \Delta z^* = 500 \text{ m}$ as originally specified by Klemp (2011). All boundary conditions are no normal flow.

The wave-shaped mountain profile has a surface height, h , given by

$$h(x) = h_0 \exp \left(- \left(\frac{x}{a} \right)^2 \right) \cos^2(\alpha x) \quad (19)$$



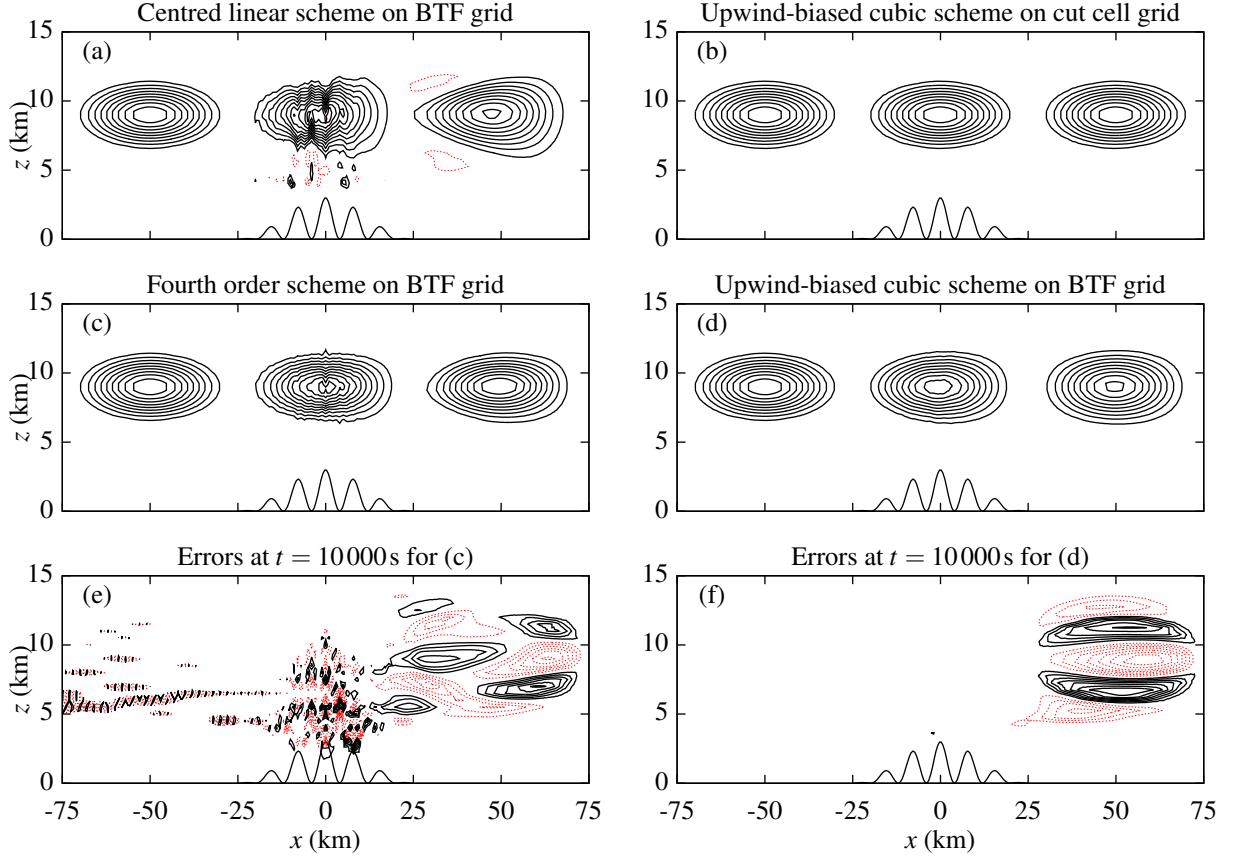


FIG. 2. Horizontally advected tracer contours at $t = 0$ s, 5000 s and 10000 s using (a) centred linear scheme on a BTF grid, the upwind-biased cubic scheme on (b) the cut cell grid, (d) the BTF grid, and (c) the fourth order scheme from Schär et al. (2002) on the BTF grid, with contour intervals every 0.1. Errors on the BTF grid at $t = 10000$ s are shown for (e) the fourth order scheme from Schär et al. (2002), and (f) the upwind-biased cubic scheme, with contour intervals every 0.01. Negative contours denoted by dotted lines. The terrain profile is also shown immediately above the x axis.

where $a = 5$ km is the mountain half-width, $h_0 = 1$ km is the maximum mountain height and $\lambda = 4$ km is the wavelength. For the optimised SLEVE grid, the large-scale component h_1 is specified as

$$h_1(x) = \frac{1}{2} h_0 \exp \left(- \left(\frac{x}{a} \right)^2 \right) \quad (20)$$

and, following Leuenberger et al. (2010), $s_1 = 4$ km is the large scale height, $s_2 = 1$ km is the small scale height, and the optimal exponent value of $n = 1.35$ is used.

The initial thermodynamic conditions are in discrete hydrostatic balance, having a reference potential temperature of $\theta(z = 0) = 288$ K and constant stability with Brunt-Väisälä frequency $N = 0.01$ s $^{-1}$ everywhere, except for a more stable layer of $N = 0.02$ s $^{-1}$ between 2 km $\leq z \leq 3$ km. Unlike Klemp (2011), there is no eddy diffusion in the equation set.

The test was integrated forward by 5 hours on the BTF, SLEVE and cut cell grids, and a regular grid with flat ter-

rain. Maximum vertical velocities are compared with the results from Klemp (2011) in figure 3 (note different vertical scales). In agreement with Klemp (2011), vertical velocities are larger on more distorted grids. However, magnitudes are smaller comparing results on the terrain following grids with those from Klemp (2011). Using the model from Weller and Shahrokhi (2014), which includes a curl-free pressure gradient formulation, w reaches a maximum of ~ 0.35 m s $^{-1}$ on the BTF grid, compared with a maximum of ~ 7 m s $^{-1}$ found by Klemp (2011) using their improved horizontal pressure gradient formulation.

Unlike the result from Klemp (2011), the SLEVE grid does not significantly reduce vertical velocities compared to the BTF grid. However, errors are three orders of magnitude smaller on the cut cell grid with vertical velocities of $\sim 1 \times 10^{-3}$ m s $^{-1}$. The smallest error of $\sim 1 \times 10^{-10}$ m s $^{-1}$ is found on the regular grid.

TABLE 1. Minimum and maximum tracer magnitudes and ℓ^2 error norms at $t = 10000$ s in the horizontal and terrain following tracer advection tests using centred linear and cubic upwind-biased schemes and, for the horizontal advection test, the fourth order scheme from Schär et al. (2002).

			Analytic	BTF	SLEVE	Cut cell	No terrain
Horizontal	Centred linear	ℓ^2 error	0	0.0210	0.00233	0.00224	0.00223
		min	0	-0.275	-0.0252	-0.0251	-0.0251
		max	1	0.925	0.985	0.985	0.985
	Fourth order	min	0	-0.0926	-0.00174	—	-0.00178
		max	1	1.00	0.984	—	0.983
	Cubic upwind-biased	ℓ^2 error	0	0.00791	0.00108	0.000577	0.000576
		min	0	-0.0446	-0.0106	-0.000674	-0.00674
		max	1	0.925	0.982	0.983	0.983
Terrain following	Centred linear	ℓ^2 error	0	0.00251	0.0173	13.6	—
		min	0	-0.0245	-0.120	-623	—
		max	1	0.985	0.950	3480	—
	Cubic upwind-biased	ℓ^2 error	0	0.00154	0.0120	0.0134	—
		min	0	-0.0110	-0.0263	-0.028	—
		max	1	0.983	0.865	0.851	—

Good et al. (2014) found the maximum vertical velocity in their cut cell model was $1 \times 10^{-12} \text{ m s}^{-1}$, which is better than any result obtained using the model by Weller and Shahrokhi (2014). It is worth noting that, in the model used by Good et al. (2014), cell centres are in the centre of the uncut cell, resulting in the centre of some cut cells being below the ground (S.-J. Lock 2014, personal communication). This means that the grid is effectively regular when calculating horizontal and vertical gradients. This would account for the very small velocities found by Good et al. (2014).

In summary, spurious velocities in the resting atmosphere test were similar on both terrain following grids, with lower errors compared to those from Klemp (2011). The maximum vertical velocity was significantly decreased on the cut cell grid, so we conclude that non-orthogonality, or lack of alignment of the grid with surfaces of constant gravitational potential are a significant cause of numerical error in this test.

d. Gravity waves

The test originally specified by Schär et al. (2002) prescribes flow over terrain with small-scale and large-scale undulations which induces propagating and evanescent gravity waves.

Following Melvin et al. (2010), the domain is 300 km wide and 30 km high. The mountain profile has the same form as equation 19. Tests are performed with mountain heights of $h_0 = 250 \text{ m}$ and $h_0 = 500 \text{ m}$. As in the resting atmosphere test, $a = 5 \text{ km}$ is the mountain half-width and $\lambda = 4 \text{ km}$ is the wavelength. On the optimised SLEVE grid, $s_1 = 5 \text{ km}$ is the large scale height, $s_2 = 2 \text{ km}$ is the small scale height and the optimal exponent value $n = 1.35$ is used.

The initial thermodynamic conditions have a surface temperature of $\theta(z = 0) = 288 \text{ K}$ and constant stability

with $N = 0.01 \text{ s}^{-1}$ everywhere. A constant horizontal wind $u = 10 \text{ m s}^{-1}$ is prescribed at the inlet boundary.

Sponge layers are added to the upper 10 km and leftmost 10 km at the inlet boundary to damp the reflection of waves. The term $\mu \rho u$ is subtracted from the momentum (equation 4a) where the damping function, μ , is adapted from Melvin et al. (2010) such that

$$\mu(x, z) = \mu_{\text{upper}} + \mu_{\text{inlet}} \quad (21)$$

$$\mu_{\text{upper}}(z) = \begin{cases} \bar{\mu} \sin^2\left(\frac{\pi}{2} \frac{z - z_B}{H - z_B}\right) & \text{if } z \geq z_B \\ 0 & \text{otherwise} \end{cases} \quad (22)$$

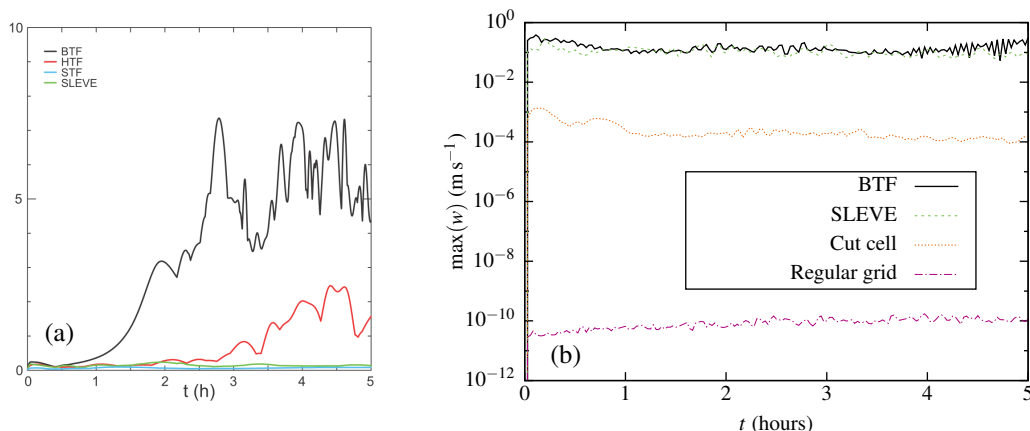
$$\mu_{\text{inlet}}(x) = \begin{cases} \bar{\mu} \sin^2\left(\frac{\pi}{2} \frac{x_I - x}{x_I - x_0}\right) & \text{if } x < x_I \\ 0 & \text{otherwise} \end{cases} \quad (23)$$

where $\bar{\mu} = 1.2$ is the damping coefficient, $z_B = 20 \text{ km}$ is the bottom of the sponge layer, $H = 30 \text{ km}$ is the top of the domain, $x_0 = -150 \text{ km}$ is the leftmost limit of the domain and $x_I = -140 \text{ km}$ is the rightmost extent of the inlet sponge layer. The sponge layer is only active on faces whose normal is vertical so that it damps vertical momentum only.

Note that, while the domain itself is 30 km in height, for the purposes of generating BTF and SLEVE grids, the domain height is set to 20 km because the sponge layer occupies the uppermost 10 km.

No normal flow is imposed at the top and bottom boundaries and the outlet has a zero gradient boundary condition. For the Exner function of pressure, hydrostatic balance is prescribed on all boundaries. The simulation is integrated forward by 5 hours with a timestep $\Delta t = 8 \text{ s}$.

Test results are compared between the BTF, SLEVE and cut cell grids. Vertical velocities on the BTF grid are shown in figure 4a, which have few visible differences from results on the SLEVE and cut cell grids (not shown). Vertical velocities on all grids are in agreement with the



Do you need to include fig 3a? If so, do you have permission from the journal

FIG. 3. Maximum spurious vertical velocity, w (m s^{-1}), in the resting atmosphere test with results on (a) BTF, SLEVE, Hybrid Terrain Following (HTF) and Smoothed Terrain Following (STF) coordinates from Klemp (2011) using their improved horizontal pressure gradient formulation, (b) BTF, SLEVE, cut cell and regular grids using the model from Weller and Shahrokh (2014) which includes a curl-free pressure gradient formulation. Note that vertical scales differ.

high resolution solution from Melvin et al. (2010), shown in figure 4b.

The initial thermal profile is subtracted from the potential temperature field at the end of the integration to reveal the structure of thermal anomalies. Once again, the results are similar on all three grids, and results are shown on the BTF and cut cell grids in figures 5a and 5c respectively. However, examining more closely the anomalies in the lee of the mountain, figure 5d shows that the bottom-most layer is anomalously warm and the layer above it is anomalously cold. This feature is not present on the BTF grid (figure 5b) or the SLEVE grid (not shown).

In a further test, the mountain height is doubled from 250 m to 500 m with all other parameter values unchanged. The same spurious anomaly in potential temperature is again present on the cut cell grid but its amplitude increases. Figure 6 shows vertical profiles of the Exner function of pressure and potential temperature in the lowest 1 km in the lee of the mountain at $x = 50$ km. We find that the Exner function of pressure decreases linearly with height on all grids. The potential temperature increases linearly with height on the BTF and SLEVE grids. On the cut cell grid, the potential temperature anomalies seen in figure 5d appear as a zig-zag in figure 6.

The inaccuracies in potential temperature become invisible when calculating momentum because θ is interpolated onto cell faces, so discrete hydrostatic balance is maintained. This is a manifestation of the Lorenz computational mode (Arakawa and Konor 1996; Holdaway et al. 2013). In models that include moist processes, the Lorenz computational mode can disrupt clouds and generate spurious precipitation (Hollingsworth 1995).

To summarize, results of the gravity waves test on all grids are in good agreement with the reference solution

from Melvin et al. (2010). The most prominent errors are found only on the cut cell grid, where the potential temperature errors near the ground excite the Lorenz computational mode.

5. Conclusions

We have presented a like-for-like comparison between terrain following and cut cell grids using a single model. Accuracy on the BTF, SLEVE and cut cell grids was evaluated in a series of two-dimensional tests.

Across all tests, a high degree of accuracy was achieved for all grids. Even on the highly-distorted BTF grid, which have previously been found to give poor results (Schär et al. 2002; Klemp 2011; Good et al. 2014), errors were often small in the tests presented here. In the first two tests, tracers were advected by horizontal and terrain following velocity fields. We found that the accuracy of the upwind-biased cubic advection scheme depended upon alignment of the flow with the grid rather than on grid distortions.

Spurious vertical velocities were small in the resting atmosphere test, reaching a maximum of $\sim 0.35 \text{ m s}^{-1}$ on the BTF grid, compared to a maximum of $\sim 10 \text{ m s}^{-1}$ found by Klemp (2011). In the gravity waves test, vertical velocities were in good agreement with the reference solution from Melvin et al. (2010) across all grids.

Cut cell grids reduced errors in two of the four tests. First, in the horizontal advection test, tracer accuracy on the cut cell grid was almost as good as accuracy on a regular grid with no mountain. Second, in the resting atmosphere test, spurious vertical velocities were two orders of magnitude smaller on the cut cell grid compared with the terrain following grids.

Conversely, in the terrain following advection test, errors were large on the SLEVE and cut cell grids where

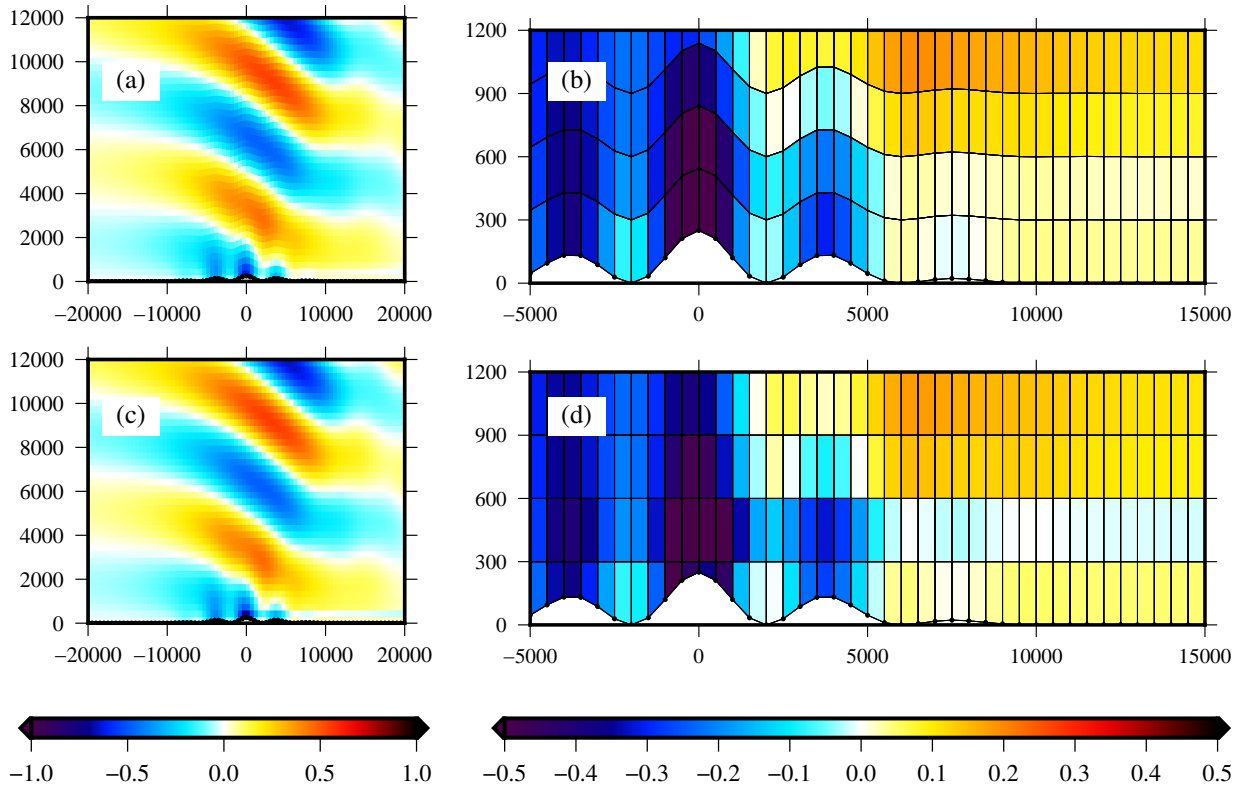


FIG. 5. Anomalies in potential temperature in the gravity waves test after 5 hours with a mountain height, $h_0 = 250$ m. The central domain in the lowest 12 km is shown on (a) the BTF grid, and (c) the cut cell grid. The four lowest layers of each grid are shown for (b) BTF, and (d) cut cell grids, using a narrower potential temperature scale. The results on the SLEVE grid (not shown) are qualitatively identical to results on the BTF grid.

velocities were misaligned with the grids. In the gravity waves test, the Lorenz computational mode was manifested as a zig-zag in potential temperature in the lowest layers in the lee of the mountain. This spurious error was excited only on the cut cell grid. This test motivates further work to formulate a Charney–Phillips staggering of variables on cut cell grids.

Acknowledgments. I am grateful to my cosupervisors John Methven and Terry Davies for their valuable input, and to Christoph Schär for his assistance in reproducing his advection test results. I am thankful for the NERC studentship which helped fund this work. Weller is funded by NERC grant NE/H015698/1.

References

- Adcroft, A., C. Hill, and J. Marshall, 1997: Representation of topography by shaved cells in a height coordinate ocean model. *Mon. Wea. Rev.*, **125**, 2293–2315.
- Arakawa, A., and C. S. Konor, 1996: Vertical differencing of the primitive equations based on the charney-phillips grid in hybrid σ – p vertical coordinates. *Mon. Wea. Rev.*, **124**, 511–528.
- Fast, J. D., 2003: Forecasts of valley circulations using the terrain-following and step-mountain vertical coordinates in the meso-eta model. *Wea. Forecasting*, **18**, 1192–1206.
- Gal-Chen, T., and R. C. Somerville, 1975: On the use of a coordinate transformation for the solution of the navier-stokes equations. *J. Comp. Phys.*, **17**, 209–228.
- Gary, J. M., 1973: Estimate of truncation error in transformed coordinate, primitive equation atmospheric models. *J. Atmos. Sci.*, **30**, 223–233.
- Good, B., A. Gadian, S.-J. Lock, and A. Ross, 2014: Performance of the cut-cell method of representing orography in idealized simulations. *Atmos. Sci. Lett.*, **15**, 44–49.
- Holdaway, D., J. Thuburn, and N. Wood, 2013: Comparison of lorenz and charney-phillips vertical discretisations for dynamics–boundary layer coupling. part ii: Transients. *Quart. J. Roy. Meteor. Soc.*, **139**, 1087–1098.
- Hollingsworth, A., 1995: *A Spurious Mode in the ‘Lorenz’ Arrangement of f and T which Does Not Exist in the ‘Charney–Phillips’ Arrangement*. European Centre for Medium-Range Weather Forecasts.
- Jebens, S., O. Knoth, and R. Weiner, 2011: Partially implicit peer methods for the compressible euler equations. *J. Comp. Phys.*, **230**, 4955–4974.

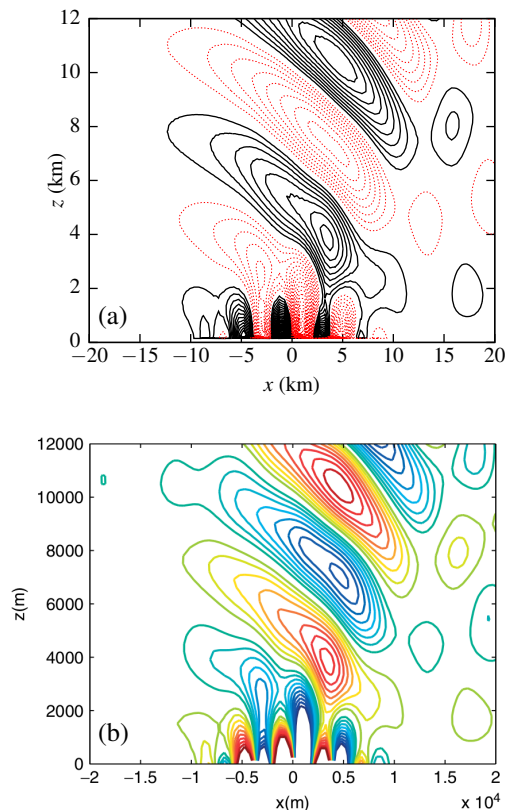


FIG. 4. Vertical cross section of vertical velocity contours in the gravity waves test after 5 hours with mountain height $h_0 = 250$ m on (a) the BTF grid compared with (b) the mass-conserving semi-implicit semi-Lagrangian solution from Melvin et al. (2010). Contours are every $5 \times 10^{-2} \text{ m s}^{-1}$ with solid lines denoting ascent and dashed lines descent. Small oscillations in contour lines are due to contouring on an irregular grid.

Klein, R., K. Bates, and N. Nikiforakis, 2009: Well-balanced compressible cut-cell simulation of atmospheric flow. *Philos. Trans. Roy. Soc. London*, **367**, 4559–4575.

Klemp, J. B., 2011: A terrain-following coordinate with smoothed coordinate surfaces. *Mon. Wea. Rev.*, **139**, 2163–2169.

Leuenberger, D., M. Koller, O. Fuhrer, and C. Schär, 2010: A generalization of the SLEVE vertical coordinate. *Mon. Wea. Rev.*, **138**, 3683–3689.

Melvin, T., M. Dubal, N. Wood, A. Staniforth, and M. Zerroukat, 2010: An inherently mass-conserving iterative semi-implicit semi-Lagrangian discretization of the non-hydrostatic vertical-slice equations. *Quart. J. Roy. Meteor. Soc.*, **136**, 799–814.

OpenCFD Foundation, cited 2015: OpenFOAM® – User Guide. [Available online at <http://cfd.direct/openfoam/user-guide/snappyhexmesh/#x26-1510005.4>].

Phillips, N. A., 1957: A coordinate system having some special advantages for numerical forecasting. *J. Meteor.*, **14**, 184–185.

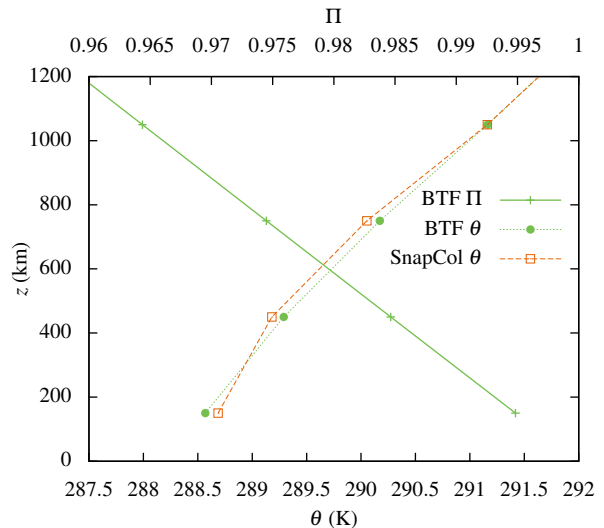


FIG. 6. Vertical profiles of the Exner function of pressure, Π , and potential temperature, θ , in the gravity waves test with a mountain height of $h_0 = 500$ m. Exner profile is visually identical on all grids for both mountain heights; for clarity, the Exner profile is only plotted for the BTF grid. The computational mode is manifested as a zig-zag in potential temperature on the cut cell grid which. Results on the SLEVE grid (not shown) are qualitatively the same as those on the BTF grid. The thermal profile with a lesser mountain height of $h_0 = 250$ m (not shown) exhibits a computational mode with smaller amplitude.

Schär, C., D. Leuenberger, O. Fuhrer, D. Lüthi, and C. Girard, 2002: A new terrain-following vertical coordinate formulation for atmospheric prediction models. *Mon. Wea. Rev.*, **130**, 2459–2480.

Simmons, A. J., and D. M. Burridge, 1981: An energy and angular-momentum conserving vertical finite-difference scheme and hybrid vertical coordinates. *Mon. Wea. Rev.*, **109** (4), 758–766.

Steppeler, J., H.-W. Bitzer, M. Minotte, and L. Bonaventura, 2002: Nonhydrostatic atmospheric modeling using a z -coordinate representation. *Mon. Wea. Rev.*, **130**, 2143–2149.

Steppeler, J., R. Hess, U. Schättler, and L. Bonaventura, 2003: Review of numerical methods for nonhydrostatic weather prediction models. *Meteor. Atmos. Phys.*, **82**, 287–301.

Steppeler, J., S.-H. Park, and A. Dobler, 2013: Forecasts covering one month using a cut-cell model. *Geosci. Model Dev.*, **6**, 875–882.

Webster, S., A. Brown, D. Cameron, and C. Jones, 2003: Improvements to the representation of orography in the met office unified model. *Quart. J. Roy. Meteor. Soc.*, **129**, 1989–2010.

Weller, H., and A. Shahrokhi, 2014: Curl free pressure gradients over orography in a solution of the fully compressible euler equations with implicit treatment of acoustic and gravity waves. *Mon. Wea. Rev.*, **142**, 4439–4457.

Yamazaki, H., and T. Satomura, 2010: Nonhydrostatic atmospheric modeling using a combined cartesian grid. *Mon. Wea. Rev.*, **138**, 3932–3945.

Zängl, G., 2012: Extending the numerical stability limit of terrain-following coordinate models over steep slopes. *Mon. Wea. Rev.*, **140**, 3722–3733.